CELLULAR NEUROSCIENCE

Local IP_3 receptor–mediated Ca^{2+} signals compound to direct blood flow in brain capillaries

Thomas A. Longden[1,2*†], Amreen Mughal[1†], Grant W. Hennig[1,3†], Osama F. Harraz[1,7], Bo Shui[4], Frank K. Lee[4], Jane C. Lee[4], Shaun Reining[4], Michael I. Kotlikoff[4], Gabriele M. König[5], Evi Kostenis[6], David Hill-Eubanks[1], Mark T. Nelson[1,3,7*]

Healthy brain function depends on the finely tuned spatial and temporal delivery of blood-borne nutrients to active neurons via the vast, dense capillary network. Here, using in vivo imaging in anesthetized mice, we reveal that brain capillary endothelial cells control blood flow through a hierarchy of IP_3 receptor–mediated Ca^{2+} events, ranging from small, subsecond protoevents, reflecting Ca^{2+} release through a small number of channels, to high-amplitude, sustained (up to ~1 min) compound events mediated by large clusters of channels. These frequent (~5000 events/s per microliter of cortex) Ca^{2+} signals are driven by neuronal activity, which engages G_q protein–coupled receptor signaling, and are enhanced by Ca^{2+} entry through TRPV4 channels. The resulting Ca^{2+}-dependent synthesis of nitric oxide increases local blood flow selectively through affected capillary branches, providing a mechanism for high-resolution control of blood flow to small clusters of neurons.

INTRODUCTION

Capillaries are composed of endothelial cells (ECs), which also line all arteries and veins. Collectively, these vessels form a continuous vascular network that permeates all tissues of the body. Intracellular Ca^{2+} elevations in arteriolar ECs exert control over the release of potent vasodilators, such as nitric oxide (NO), which are critical for the control of blood flow and pressure (*1*). Ca^{2+} release from the endoplasmic reticulum (ER) membrane through ubiquitous inositol trisphosphate receptors (IP_3Rs) is a major pathway for increasing cytosolic Ca^{2+} levels in arteriolar ECs (*2*), an increase that can be augmented by Ca^{2+} influx across the plasmalemma through TRPV4 (transient receptor vanilloid member 4) nonselective cation channels (*3*). Although the central role of Ca^{2+} in arteriolar ECs is well established, the nature of capillary EC (cEC) Ca^{2+} signaling and its regulation in the brain and potential contribution to blood flow control are unexplored.

RESULTS

To establish an unambiguous framework for our analyses, we first defined a nomenclature for referring to the brain vasculature. We classify vessels as arterioles, venules, or capillaries according to branch order and orientation. The penetrating arteriole branching from pial arteries on the brain's surface is defined as the 0-order (0°) parenchymal arteriole, characterized by its coverage by concentric smooth muscle cells (SMCs), which secrete elastin to form an elastic lamina (*4*). We define elastin-negative vessels branching from this arteriole as capillaries (fig. S1) and further distinguish the initial ~4 branches of the capillary bed as a transition zone (*5*, *6*), reflecting the fact that these vessels have features common to both arterioles and deeper capillaries. Specifically, the narrow, proximal branches (1st- to ~4th-order; 1° to 4°) of the transition zone through which red blood cells (RBCs) pass in single file are heavily covered with processes of α-actin–positive contractile cells whose cell bodies display a characteristic "bump-on-a-log" morphology (*7*). These cells have been variably referred to as SMCs (*8*, *9*), contractile pericytes (*10*), or a hybrid cell type (*11*, *12*). Here, we use the term "contractile pericyte." Deeper capillaries (≥5th order; ≥5°) are in contact with the thin-strand processes of noncontractile pericytes, which express little or no smooth muscle α-actin (*5*–*7*). The first large-diameter (>7 μm), vertically oriented vessel carrying blood back to the brain's surface is designated as a venule.

To study Ca^{2+} signaling in the capillary network, we developed a transgenic mouse line in which GCaMP8, a high signal-to-noise Ca^{2+} indicator, is expressed under transcriptional control of the pan-endothelial *Cdh5* (cadherin 5) promoter as part of a bacterial artificial chromosome (*13*). The resulting $Cdh5^{BAC}$-GCaMP8 mice express this indicator exclusively in vascular ECs throughout all observed vascular beds (fig. S2), allowing us to isolate cEC Ca^{2+} signals. To study these signals in the cortex, we created a cranial window by surgically removing the skull overlying the barrel cortex, resecting the dura, and attaching a head plate for immobilization. We then illuminated plasma by delivering TRITC-dextran (tetramethylrhodamine isothiocyanate–dextran) to the bloodstream to enable simultaneous visualization of blood flow and endothelial Ca^{2+} activity using two-photon laser scanning microscopy. To analyze Ca^{2+} signals in vascular structures, we mapped wide areas of the somatosensory cortical vasculature down to approximately layer III before selecting a volume of interest and then performed nested "four-dimensional" (4D) imaging, consisting of repeated temporal sweeps through cuboidal volumes measuring ~425 μm by 425 μm by 50 μm. This volumetric approach provides information on EC Ca^{2+} activity over a broad spatial region over time. To permit temporal analysis of individual Ca^{2+} events, we followed this by imaging a ~425 μm–by–425 μm single *xy* plane from within the same region with subsecond resolution (Fig. 1A). Brain ECs in all segments of the vasculature

[1]Department of Pharmacology, University of Vermont, Burlington, VT, USA. [2]Department of Physiology, School of Medicine, University of Maryland, Baltimore, MD, USA. [3]Vermont Center for Cardiovascular and Brain Health, University of Vermont, Burlington, VT, USA. [4]Department of Biomedical Sciences, College of Veterinary Medicine, Cornell University, Ithaca, NY, USA. [5]Institute of Pharmaceutical Biology, University of Bonn, 53115 Bonn, Germany. [6]Molecular, Cellular, and Pharmacobiology Section, Institute of Pharmaceutical Biology, University of Bonn, 53115 Bonn, Germany. [7]Division of Cardiovascular Sciences, University of Manchester, Manchester, UK.
*Corresponding author. Email: mark.nelson@uvm.edu (M.T.N.); thomas.longden@som.umaryland.edu (T.A.L.)
†These authors contributed equally to this work as co–first authors.

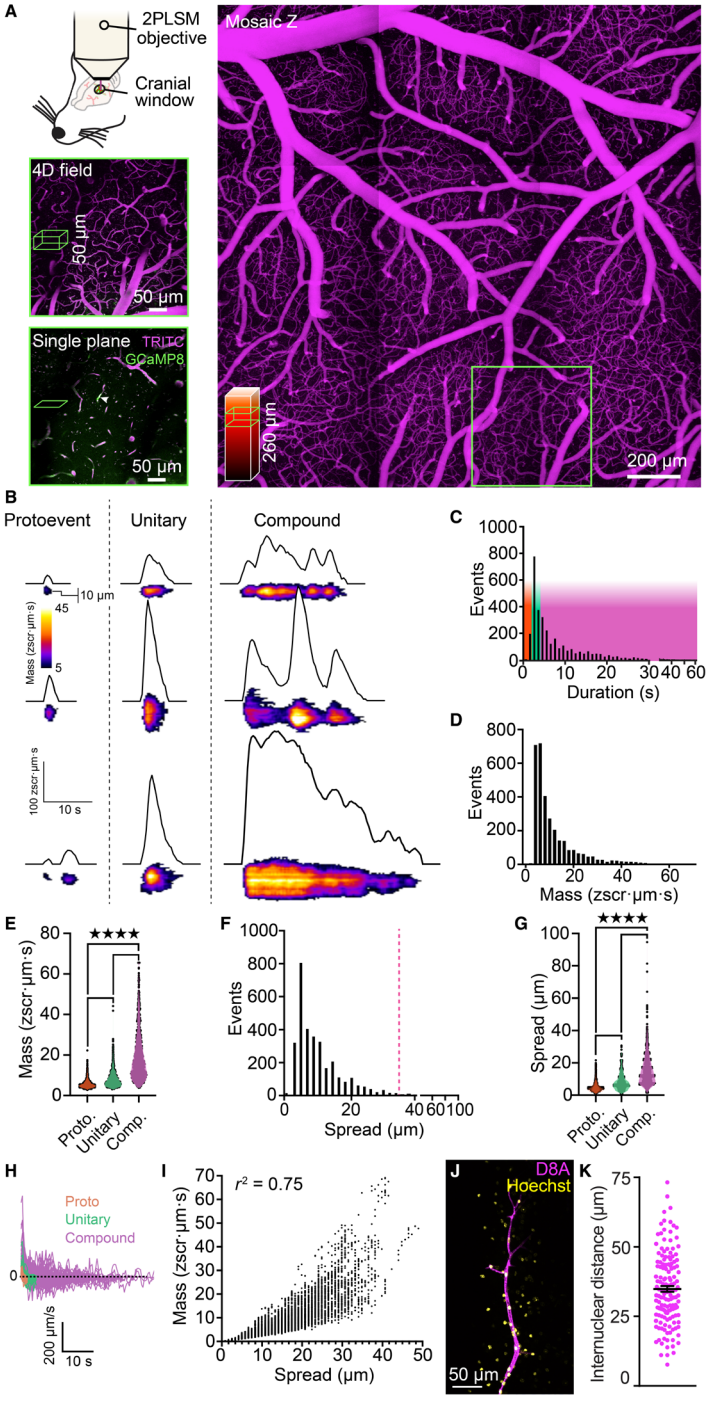

Fig. 1. Dynamic Ca^{2+} signaling in the brain endothelium. (**A**) In vivo imaging strategy. Top left: A cranial window was centered over the somatosensory region, imaged using two-photon laser scanning microscopy. Left: Vascular field mapped from luminal TRITC-dextran. Bottom left: Region around a penetrating arteriole imaged at higher resolution, selected for 4D imaging, and a single plane, within the 4D block of interest above. Magenta, TRITC-dextran; green, GCaMP8. (**B** to **I**) Characterization of cEC Ca^{2+} events (proto, $n = 1184$ events; unitary, $n = 786$; compound, $n = 1257$). (B) Capillary Ca^{2+} events ranging from proto events to unitary singlets and multicomponent compound events. (C) Durations for all events analyzed. Color overlay indicates event classes: red, proto; green, unitary; magenta, compound. (D) Amplitudes for all events analyzed. (E) Event mass by class [$P < 0.0001$ ($q_{3224} = 10.76$), proto versus unitary; $P < 0.0001$ ($q_{3224} = 43.89$), unitary versus compound; $P < 0.0001$ ($q_{3224} = 61.51$), compound versus proto; one-way analysis of variance (ANOVA) and Tukey's multiple comparisons test]. (F) Lengths of cEC Ca^{2+} events. The dashed line indicates the average length of a cEC [from (K)]. (G) Event length by class [$P < 0.0001$ ($q_{3224} = 15.25$), proto versus unitary; $P < 0.0001$ ($q_{3224} = 34.45$), unitary versus compound; $P < 0.0001$ ($q_{3224} = 56.01$), compound versus proto; one-way ANOVA and Tukey's multiple comparisons test]. (H) Event spread velocity by class. Deviation above the line represents event expansion, whereas below the line represents contraction. (I) Relationship between cEC Ca^{2+} event mass and spread. (**J**) Di-8-ANEPPS (magenta) and Hoechst 33342 (yellow) staining of the capillary endothelium and cEC nuclei. (**K**) Internuclear distances measured using Di-8-ANEPPS and Hoechst 33342 ($n = 150$ measurements, 3 mice).

displayed dynamic local Ca^{2+} events under basal conditions in vivo (movie S1) that were notable for their striking amplitudes and long durations.

A hierarchy of capillary Ca^{2+} events provides an enormous dynamic range of cEC Ca^{2+} signaling

The standard F/F_0 approach to Ca^{2+} analysis, in which experimentally induced increases in the fluorescence of Ca^{2+} indicators are expressed relative to prestimulus (baseline) fluorescence, has been very useful in characterizing Ca^{2+} signals in a broad range of cells. However, it has a number of limitations that compromise accurate characterization of dynamic fluorescence changes. To resolve and analyze brain cEC Ca^{2+} transients with greater accuracy and precision, we developed a novel autonomous image analysis approach based on signal-to-noise ratios and statistical *z* scores (zscr) and combined this with spatiotemporal (ST) mapping (figs. S3 and S4 and Materials and Methods). To accurately quantify event mass, we developed a novel unit (zscr·μm·s) that encapsulates pixel intensity throughout the entire spatial area of an event over time (see Materials and Methods). This approach provides a distinct advantage over the traditional F/F_0 analysis in that it enables accurate assessment of event amplitude independent of varying levels of background fluorescence and incorporates intensity data across ST domains. Moreover, this approach permits the reliable detection of even very small fluorescence changes. Bringing these tools to bear on our analysis of capillary Ca^{2+} signals occurring under basal conditions in anesthetized mice (α-chloralose and urethane), we observed a spectrum of Ca^{2+} event types that we categorized into three classes according to distinct features and temporal characteristics (Fig. 1, B to I). At one end of the spectrum, we were able to routinely resolve very small Ca^{2+} events, which we termed "protoevents." These brief, low-amplitude events, which represented single-point sources of local Ca^{2+} release (Fig. 1B), accounted for 36.6% of Ca^{2+} events recorded under basal conditions and exhibited an average duration of 1.95 ± 0.02 s (Fig. 1C), a rise time of 433 ± 35 ms, and a mass of 5.71 ± 0.06 zscr·μm·s (Fig. 1E and movie S2). A second class of events, which we termed "unitary Ca^{2+} events," exhibited a consistent spike-like waveform (Fig. 1B) with a rapid rise time from baseline of 313 ± 14 ms, a mean duration of 4.24 ± 0.03 s, and an average mass of 8.46 ± 0.16 zscr·μm·s (Fig. 1, C to E, and movie S2). These events accounted for 24.4% of events recorded. The remaining ambient events, accounting for ~39% of the total, were much larger and longer than unitary Ca^{2+} events and exhibited multiple peaks and fluctuating plateaus, suggesting that these events actually reflect the compounding of a series of protoevents and unitary Ca^{2+} transients (Fig. 1B and movie S2). We found that these larger events, which we refer to as "compound Ca^{2+} events," consisted of two or more proto- and unitary events that summed to produce complex waveforms reflecting the interval between transients, their amplitudes, and their spatial locations within the cEC. Some events were composed of Ca^{2+} delivered via distinct clusters of spatially separated point sources, likely representing the activity of small groups of cEC ion channels. On average, clusters were separated by 5.15 ± 0.22 μm (n = 90 clusters, 37 mice), and up to 4 distinct clusters could be recruited during a compound event. As a population, compound events lasted on average 16.17 ± 0.38 s, exhibited an average mass of 19.56 ± 0.34 zscr·μm·s (Fig. 1, C to E), and showed an increase in mass and duration with an increasing degree of compounding (r^2 = 0.4226, P < 0.0001; n = 3227 events). The minimum detected Ca^{2+} output of a protoevent was ~0.7 zscr·μm·s, and the Ca^{2+} output of the largest compound event observed in a cEC was approximately 7400 zscr·μm·s—a 10,000-fold range of Ca^{2+} signal magnitude. Signal durations also spanned a considerable range, from subsecond protoevents to compound events lasting almost 1 min.

Despite this elaborate repertoire of events, on average, an active site—a contiguous spatial area of a capillary in which one or more Ca^{2+} events were detected—exhibited Ca^{2+} elevations for only 5.0 ± 0.8% of a recording period, with just over a third (35.7%) of all sites (n = 987 sites, 44 mice) exhibiting only a single event during a typical ~4-min recording epoch. To better appreciate cEC Ca^{2+} event prevalence, we analyzed event frequency across the total length of capillaries in each field and extrapolated this to a standardized 1-mm length of capillary. This analysis yielded frequencies of 178 ± 24 events/min per millimeter for protoevents, 136 ± 23 events/min per millimeter for unitary events, and 237 ± 17 events/min per millimeter for compound events (n = 7 mice). Thus, events arose frequently throughout the capillary network but were often followed by a substantial quiescent period at any one site. An analysis of the frequency of events per individual capillary segment confirmed this, revealing 0.71 protoevents events per capillary per minute, 0.26 unitary events per capillary per minute, and 0.31 compound events per capillary per minute (n = 18 mice). A further analysis of cortical angioarchitecture undertaken to place these data in context revealed a total vascular length of 0.636 ± 0.113 m/μl of cortex in our recordings (n = 7 volumes from 7 mice). Assuming that the capillary bed comprises 85% of this by volume (*14*), our data indicate that the capillaries in this region exhibit a notable ~297,000 Ca^{2+} events/min or roughly 5000 events/s.

To determine whether proto-, unitary, and compound Ca^{2+} events occur in restricted regions of cECs or spread over longer distances and into adjacent cells, we assessed their ST characteristics. This analysis indicated that protoevents occupied small regions of capillaries (average event length, 4.94 ± 0.09 μm), suggesting that they result from a small number of channels, whereas unitary events were ~65% larger (8.21 ± 0.18 μm), consistent with the activity of more channels. Compound events, in contrast, were more than three times the size of protoevents (15.49 ± 0.26 μm; Fig. 1, F and G). Notably, events in all classes initially exhibited a high release velocity (Fig. 1H); in the case of unitary and compound events, this resulted in explosive spread (Fig. 1B) suggestive of the rapid recruitment of multiple channel clusters. This was quickly followed by an exponential decay in the rate of expansion, leading to gradual contraction of the event, presumably as Ca^{2+} was cleared from the cytosol. For compound events, peak expansion velocity occurred at 0.785 s and averaged 53.2 ± 4.0 μm/s [decay time constant (τ) = 1.49 s; n = 256 events, 42 mice]. The peak spreading velocity of unitary events averaged 37.5 ± 3.5 μm/s (τ = 0.90 s; n = 84 events, 42 mice), whereas protoevents expanded at an average velocity of 17.95 ± 1.32 μm/s (τ = 1.01 s; n = 126 events, 42 mice). Event spread could be reliably predicted by event mass (Fig. 1I), indicating that the spatial coverage of an event is a linear function of the amount of Ca^{2+} initially entering the cytosol. Intracellular spread typically stopped abruptly at sharply defined apparent boundaries, suggesting a physical limitation imposed by the cell membrane at cell-cell borders (movie S3).

To further understand the relationship between the spatial characteristics of cEC Ca^{2+} events and the angioarchitecture of the capillary network, we first quantified branch points within a cortical vascular volume of GCaMP8 mice using our 4D imaging approach.

This analysis yielded a branch point density of 4924 ± 584/mm^3 (n = 7 volumes from 7 mice). On average, capillary branch points were separated by a length of vasculature measuring 35.6 ± 5.5 μm (fig. S5), a value comparable to that observed in C57BL6 mice (fig. S6). To relate this to the length of cECs, we measured the average cEC internuclear distance in brain slices from mice transcardially perfused with the vital nuclear stain Hoechst 33342 and Di-8-ANEPPS, a dye that binds to the cell membrane and outlines the entirety of the intracerebral vasculature (Fig. 1J). This analysis revealed that the average capillary length between two cEC nuclei is 34.9 ± 1.0 μm (Fig. 1K), equivalent to the length of a single capillary between branch points and longer than ~99% of all Ca^{2+} events observed (Fig. 1F). An analysis of the distribution of Ca^{2+} events according to position within the capillary angioarchitecture revealed no differences in activity between branch points and nonbranching capillary segments (n = 104 to 163 observations, 18 mice). Because distinct segments of the vascular network functionally and morphologically differ, we further compared the distribution of events according to capillary branch order (fig. S7). This analysis revealed that, although proto-events were frequent at all branch points, the proportions of unitary and compound events changed as a function of branch order. Specifically, the distribution of these events was significantly different between first- and second-order capillaries but showed no further differences among second-, third-, and fourth-order capillaries. The preponderance of compound and unitary events was greater in fifth-order capillaries than in first- to fourth-order vessels. Collectively, these analyses indicate that brain cEC Ca^{2+} events can be stratified into three distinguishable types and strongly suggest that they are restricted to subdomains of single cECs.

Neuronal activity modulates capillary Ca^{2+} events to shape their spread and duration

To determine whether cEC Ca^{2+} events observed under nonstimulated conditions are dependent on neuronal activity, we recorded Ca^{2+} signals before and after inhibiting neuronal activity with the selective voltage-dependent Na^+ channel blocker, tetrodotoxin (TTX; 3 μM), applied to the cortical surface. TTX treatment produced a notable decrease in Ca^{2+} events at all active sites (Fig. 2, A and B, and movie S4); in contrast, time control experiments showed no difference in cEC Ca^{2+} events over 30 min (fig. S8). Thus, our data suggest that neural activity underpins the elaboration of ambient cEC Ca^{2+} events.

To test whether direct engagement of neural activity evokes an increase in EC Ca^{2+} signaling, we investigated how increasing the activity of neurons in the primary somatosensory cortex using electrical forepaw stimulation (FPS) affected Ca^{2+}. Notably, FPS evoked rapid and robust increases in both arteriolar and cEC Ca^{2+} (Fig. 2, C to E, and movie S5) in association with an increased prevalence of events throughout the arteriole-proximal region of the capillary bed (first- to third-order segments downstream of the feeding arteriole). These events were accompanied by increases in capillary blood flow, measured as RBC flux using high-frequency line scanning (fig. S9). Response latencies and Ca^{2+} event amplitudes and durations in arterioles and first- to third-order capillaries were equally robust, with FPS evoking compound Ca^{2+} events that initiated within 2.3 ± 0.3 s and lasted on average 15.8 ± 1.4 s (n = 97 events, 22 mice). Collectively, these data support the conclusion that neuronal activity can rapidly increase EC Ca^{2+} signaling in vivo.

Activation of IP_3Rs and TRPV4 channels by G_qPCR signaling underpins capillary Ca^{2+} signaling

We next sought to determine the mechanism driving cEC Ca^{2+} signaling. cECs express a range of G_q protein–coupled receptors (G_qPCRs) that impart an ability to detect a variety of potential agonists released by active neurons and astrocytes. Accordingly, we tested the effect of the selective $G_{q/11}$ inhibitory depsipeptide, FR900359 (10 μM) (*15*), on cEC signaling. Notably, this agent nearly abolished capillary Ca^{2+} activity, reducing the number of events by 90% (Fig. 3, A to C, and movie S6) and similarly affecting proto-, unitary, and compound events (Fig. 3D). The few residual events that remained after this treatment exhibited ST profiles typical of all three classes, implying that G_qPCR signaling is crucial for the initiation of cEC Ca^{2+} events but not their subsequent evolution. Given the putative role of prostaglandin E_2 (PGE_2) in neurovascular coupling (*16*), we reasoned that prostaglandins might act through the G_q-coupled capillary EP_1 receptor to drive cEC Ca^{2+} events. Consistent with this possibility, localized, low-pressure ejection of PGE_2 (1 μM) onto cECs of capillaries in vivo in the presence of TTX produced robust increases in cEC Ca^{2+} and increased blood flow (fig. S10), whereas ejection of artificial cerebrospinal fluid (aCSF; vehicle) alone had no effect (Fig. 3, E to H).

Cell surface G_qPCRs convert phosphatidylinositol 4,5-bisphosphate (PIP_2) to IP_3 and diacylglycerol (DAG) through the action of phospholipase C (PLC) (*17*). IP_3 binding to IP_3Rs on the ER membrane increases the sensitivity of its cognate receptor to cytosolic Ca^{2+}, leading to IP_3R opening and release of Ca^{2+} from the ER (*2*). To confirm a key role for IP_3Rs in cEC signaling, we depleted ER Ca^{2+} stores by inhibiting the activity of the sarco-ER Ca^{2+} ATPase pump with cyclopiazonic acid (CPA; 0.7 mg/kg) delivered intravenously. As anticipated, this maneuver caused a large reduction in cEC Ca^{2+} activity (Fig. 3I and movie S7). Intravenous delivery of the selective IP_3R inhibitor xestospongin C (0.45 mg/kg) or 2-aminoethyl diphenylborinate (2-APB; 1.12 mg/kg), which also inhibits IP_3Rs, similarly reduced overall Ca^{2+} activity, decreasing it by 52% (Fig. 3, J and K) and 54% (fig. S11A), respectively. These data support the idea that cEC Ca^{2+} events are predominantly IP_3R-mediated, leading us to postulate that Ca^{2+} from these events spreads through an IP_3R-mediated Ca^{2+}-induced Ca^{2+} release (CICR) process. To test this concept, we chelated intracellular Ca^{2+} released from the ER via IP_3Rs using EGTA (0.55 mg/kg), delivered into the bloodstream as an acetoxymethyl ester to enable its penetration into and accumulation within the endothelium. As predicted, this maneuver reduced overall Ca^{2+} activity and led to a reduction in the spatial spread of events, implying that CICR contributes to the triggering and spatial evolution of events (Fig. 3, I to K, and movie S8).

In parallel with increases in IP_3-mediated Ca^{2+} release, PIP_2 depletion resulting from G_qPCR engagement of PLC disinhibits TRPV4 channels (*18*), causing local elevation of Ca^{2+} levels (*3*). We reasoned that the resulting increase in TRPV4 activity could increase Ca^{2+} entry and activate IP_3Rs in cECs via a CICR mechanism, thereby contributing to event initiation and evolution. Consistent with this supposition, the TRPV4 channel agonist GSK1016790A (1 μM) increased the number of events across all classes (Fig. 3, L and M, and movie S9). Although G_qPCR activation increases the activity of TRPV4 channels ~6-fold, their total open probability (NPo) is still exceedingly low (NPo = 0.038), corresponding to less than one channel open at a given moment across the entire cell membrane

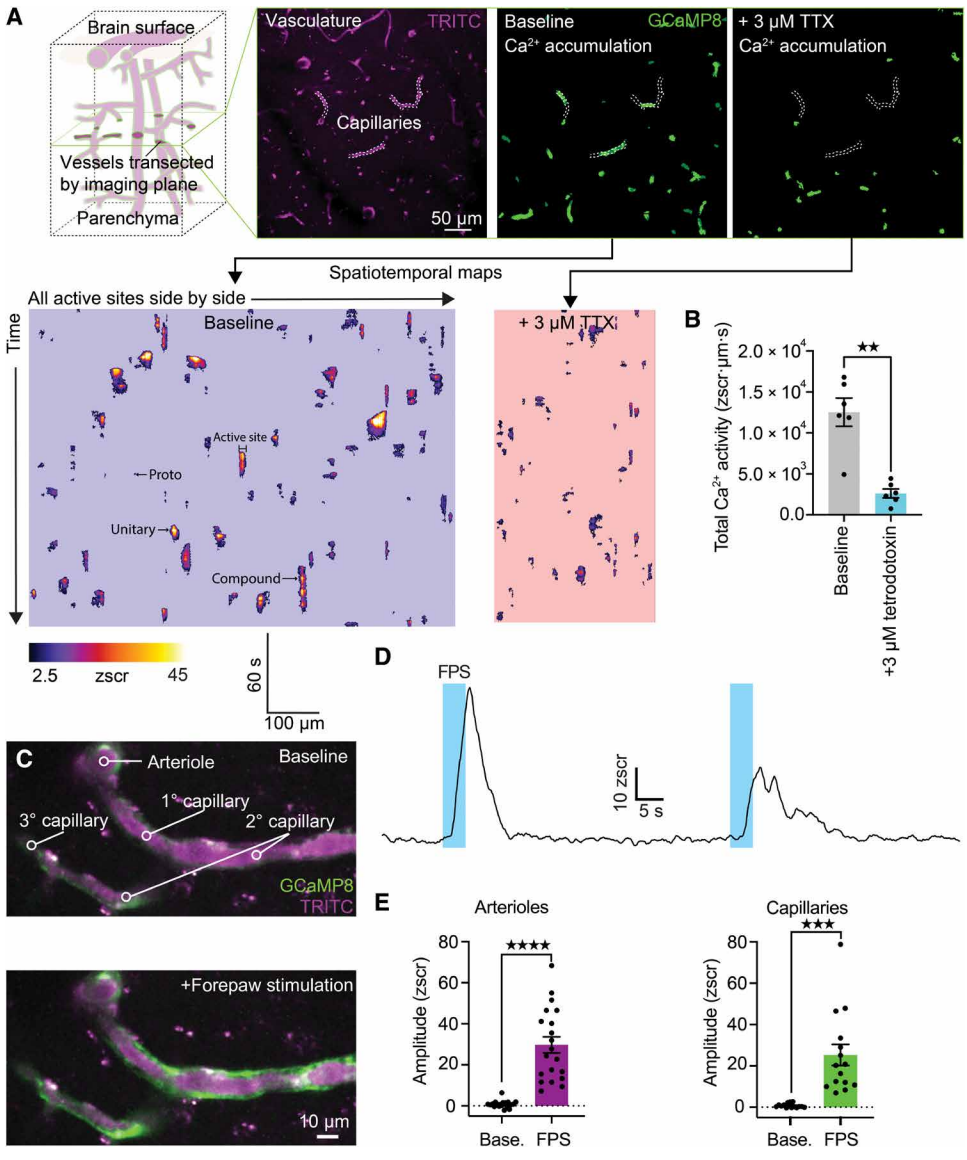

Fig. 2. TTX suppresses brain cEC Ca^{2+} signaling in vivo. (**A**) Top left: Imaging outline. A single optical section through a field of vessels within the brain was imaged for 236 s. Top right three panels: Typical field showing TRITC-dextran–filled vasculature (magenta; left) and accumulation plots showing all Ca^{2+} activity recorded in this plane under baseline conditions (middle) and all activity in the same field after the addition of 3 μM TTX (right). Bottom: Recordings converted to ST maps, total length of all active sites are side by side on the *x* axis and time on the *y* axis (left), and the effects of TTX (right). TTX decreases in the number of active sites, which reduces the length of the *x* axis, and decreases in event amplitudes and durations appear as smaller individual events in the *y* axis. (**B**) Summary data showing the effects of TTX on total Ca^{2+} activity in each field [$n = 6$ experiments, 6 mice; $P = 0.0038$ ($t_5 = 5.091$), paired Student's *t* test]. (**C**) Sensory stimulation engages arteriolar and capillary Ca^{2+} signals. Top: A single plane through the penetrating arteriole and the connected first- to third-order capillaries. Bottom: Electrical FPS–induced increases in Ca^{2+} in arteriolar ECs and cECs. (**D**) Traces from an individual experiment showing robust responses of capillaries and arterioles to FPS across two trials separated by ~1 min. (**E**) Summary showing Ca^{2+} signals evoked by neural activity in the penetrating arteriole [$n = 19$ paired experiments; $P < 0.0001$ ($t_{18} = 7.685$), paired Student's *t* test] and capillaries [$n = 15$ paired experiments; $P = 0.0003$ ($t_{14} = 4.699$), paired Student's *t* test].

(*18*). Despite this limited activity profile, inhibition of TRPV4 channels with the potent and selective TRPV4 channel antagonist, GSK2193874 (100 nM), reduced cEC Ca^{2+} activity (Fig. 3N and movie S10). In particular, this maneuver targeted compound events (fig. S11B), suggesting an important role for TRPV4 in promoting the development of these larger events.

In complex tissues, the locus of action of pharmacological agents can be difficult to discern. Accordingly, we cannot, at present, rule out the effects of these maneuvers on neurons and glia. However, the simplest explanation for our data, together, is that G_qPCR signaling simultaneously engages both IP_3Rs and TRPV4 channels in cECs, establishing these two channels as fundamental molecular players underpinning cEC Ca^{2+} events. Our data further indicate that Ca^{2+} release through IP_3R-mediated protoevents self-amplifies by recruiting further events through CICR, while Ca^{2+} entry through TRPV4 also contributes to this process.

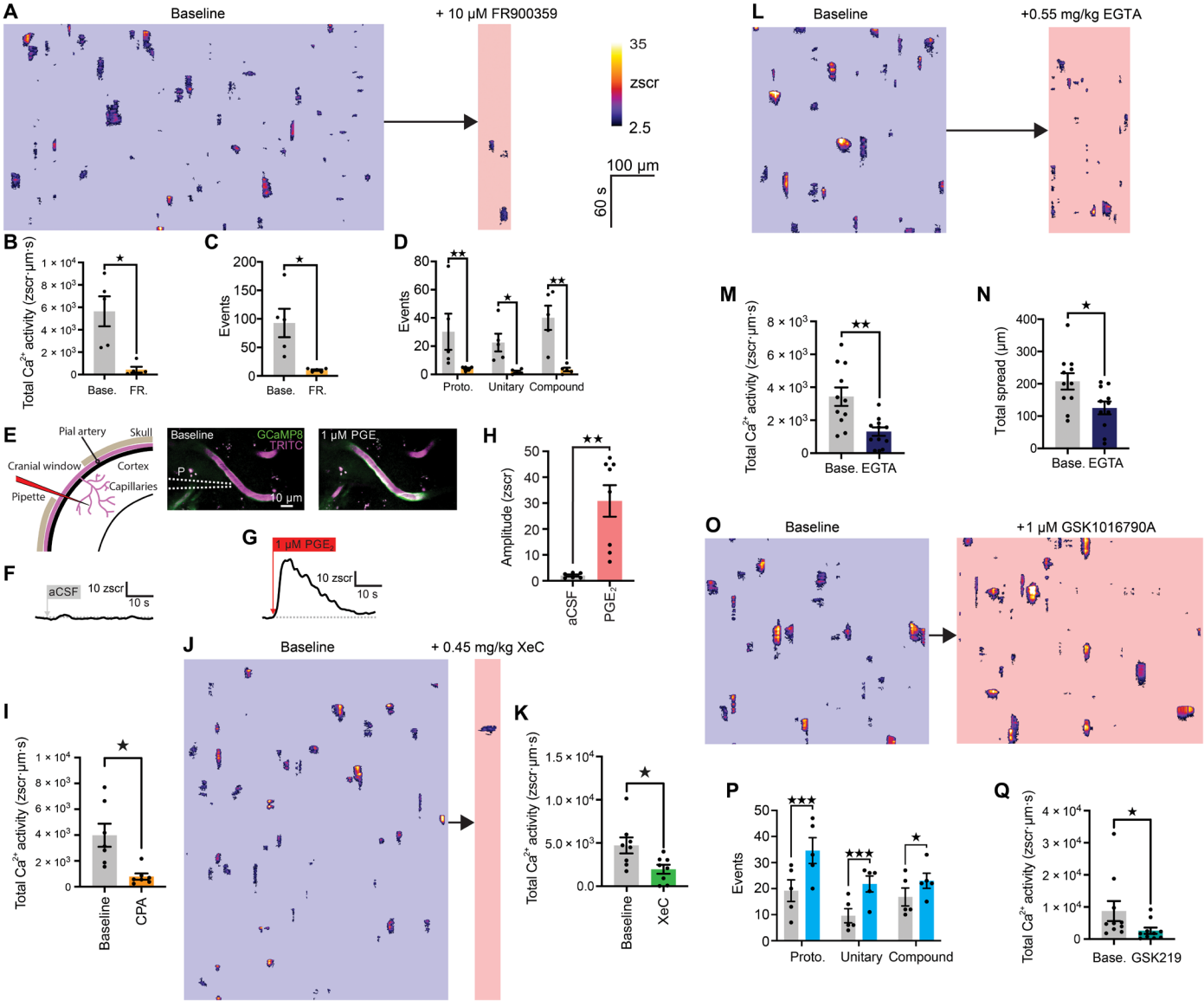

Fig. 3. G_qPCR signaling through IP_3Rs and TRPV4 drives cEC Ca^{2+} signaling. (**A**) ST maps before/after FR900359. Scale bars apply to all maps. (**B**) FR900359 on cEC Ca^{2+} activity [$n = 5$ experiments, 5 mice; $P = 0.0147$ ($t_4 = 4.117$), paired t test], (**C**) total events [$n = 5$ experiments, 5 mice; $P = 0.0282$ ($t_4 = 3.364$), paired t test], and (**D**) events by class [$n = 5$ experiments, 5 mice; proto, $P = 0.0064$ ($t_8 = 4.445$); unitary, $P = 0.023$ ($t_8 = 3.522$); compound, $P = 0.0008$ ($t_8 = 6.223$); two-way ANOVA and Sidak's multiple comparisons test]. (**E**) Focal application of PGE_2 on cEC Ca^{2+}. Left: Pipette (P) position. Right: Peak cEC Ca^{2+} after PGE_2. (**F**) No Ca^{2+} response of a capillary to aCSF, and an increase in Ca^{2+} following PGE_2 (**G**). (**H**) Summary [$n = 6$ to 8 experiments, 3 to 5 mice; $P = 0.0016$ ($t_{12} = 4.054$), unpaired t test]. (**I**) CPA decreased Ca^{2+} activity [$n = 7$ experiments, 7 mice; $P = 0.0178$ ($t_6 = 3.233$); paired t test]. (**J** and **K**) Reduction in Ca^{2+} activity by xestospongin C [$n = 8$ experiments, 8 mice; $P = 0.0318$ ($t_7 = 2.675$); paired t test]. (**L** to **N**) Maps and summary for EGTA-mediated changes in Ca^{2+} activity [$n = 11$ experiments, 11 mice; $P = 0.0090$ ($t_{10} = 3.230$), paired t test] and spatial spread [$n = 11$ experiments, 11 mice; $P = 0.0415$ ($t_{10} = 2.337$), paired t test]. (**O**) ST map of TRPV4 activation with GSK1016790A. (**P**) TRPV4 activation on event classes [$n = 5$ experiments, 5 mice; proto, $P = 0.0001$ ($t_8 = 8.102$); unitary, $P = 0.0006$ ($t_8 = 6.418$); compound, $P = 0.0341$ ($t_8 = 3.262$); two-way ANOVA and Sidak's multiple comparisons test]. (**Q**) Inhibition of TRPV4 with GSK2193874 [$n = 10$ experiments, 10 mice; $P = 0.0303$ ($t_9 = 2.567$), unpaired t test].

Kir2.1-mediated electrical signaling is a key modulator of capillary Ca^{2+} signaling

We previously established that Kir2.1-mediated electrical signals are major controllers of blood flow through capillaries (*19*). These rapid hyperpolarizing signals are generated in response to neuronally released K^+ and are passed via gap junctions from capillaries to upstream arterioles to drive robust membrane hyperpolarization and smooth muscle relaxation. We hypothesized that the hyperpolarization resulting from these signals would increase the driving force for Ca^{2+} entry across the plasmalemma of cECs, thereby amplifying capillary Ca^{2+} signaling. In our previous study, we measured membrane potential in SMCs upstream of capillaries stimulated with 10 mM K^+, demonstrating a 23-mV hyperpolarization (*19*). For a similar change in the electrochemical gradient (i.e., 20 mV), the Goldman-Hodgkin-Katz equation predicts a doubling in the driving force for Ca^{2+} influx (*20*). Notably, we found that the Kir2.1 blocker Ba^{2+} reduced capillary Ca^{2+} signaling by 80% (Fig. 4, A to C). These data are consistent with the idea that ongoing electrical signaling is essential for Ca^{2+}

entry into the capillary endothelium and strongly imply that electrical and Ca^{2+} signaling are intimately linked, operating in tandem to control blood flow. The exact mechanisms through which this linkage operates are unknown and are the subject of our ongoing investigations.

Ca^{2+} events generate NO to tune blood flow within the capillary bed

A single penetrating arteriole perfuses a cylindrical volume of the parenchyma of ~0.22 mm^3 (*21*), a volume that encompasses approximately 20,000 neurons (*22*). According to the analysis herein, this volume contains ~0.15 m of blood vessels that diverge and converge at ~1100 branch points, and the cECs within it collectively exhibit ~1200 local Ca^{2+} events/s. This angioarchitecture and the astounding array of capillary Ca^{2+} events beg an important question: Is the spatial control of RBC delivery limited to the broad perfusion domain fed by a penetrating arteriole, or are these Ca^{2+} events involved in a local regulatory mechanism that finely controls RBC distribution within the capillary bed downstream of the penetrating arteriole?

The post-arteriole transitional zone of the capillary bed is preceded by a dynamically regulated precapillary sphincter (*23*), and the first ~2 to 4 capillary segments downstream of the feeding arteriole are covered by α-actin–expressing contractile pericytes (*5*–*7*), which have been reported to play an important role in controlling capillary blood flow (*5*, *10*, *24*). Ca^{2+} elevations in such contractile cells often directly trigger actin-myosin crossbridge cycling (*25*). In contrast, Ca^{2+} elevations in arteriolar ECs routinely produce relaxation of adjacent SMCs through production of multiple signaling mediators (*26*). To assess the effects of cEC Ca^{2+} elevation on blood flow, we measured RBC flux at junctions in first- to third-order branches of the capillary bed using high-frequency line scans (Fig. 5, A and B) and related this flux to simultaneously recorded ambient cEC Ca^{2+} events occurring in the capillary wall. This latter approach revealed robust compound Ca^{2+} events at these transitional zone locations under basal conditions, 89% of which were temporally associated with a profound increase in RBC flux (peak increase versus basal, 30 ± 5 RBCs/s; latency from Ca^{2+} event onset to onset of an increase in flux, 4.1 ± 0.6 s; n = 18 experiments, 9 mice; Fig. 5, B, C, and E, and fig. S12, A to D). Anesthesia may affect this latency; thus, these dynamics may be more rapid in awake animals. Ambient Ca^{2+} signals occurring deeper in the capillary bed (≥5th-order branches) were not associated with increases in blood flow (Fig. 5E and fig. S12, E to G). This observation dovetails with previous findings that pericytes at deeper levels of the vascular tree lack contractile actin (*5*–*7*) and implies that proximity to contractile pericytes in the arteriole-adjacent region of the capillary bed is necessary for functional linkage of cEC Ca^{2+} events to increases in RBC flux. In cases where concurrent

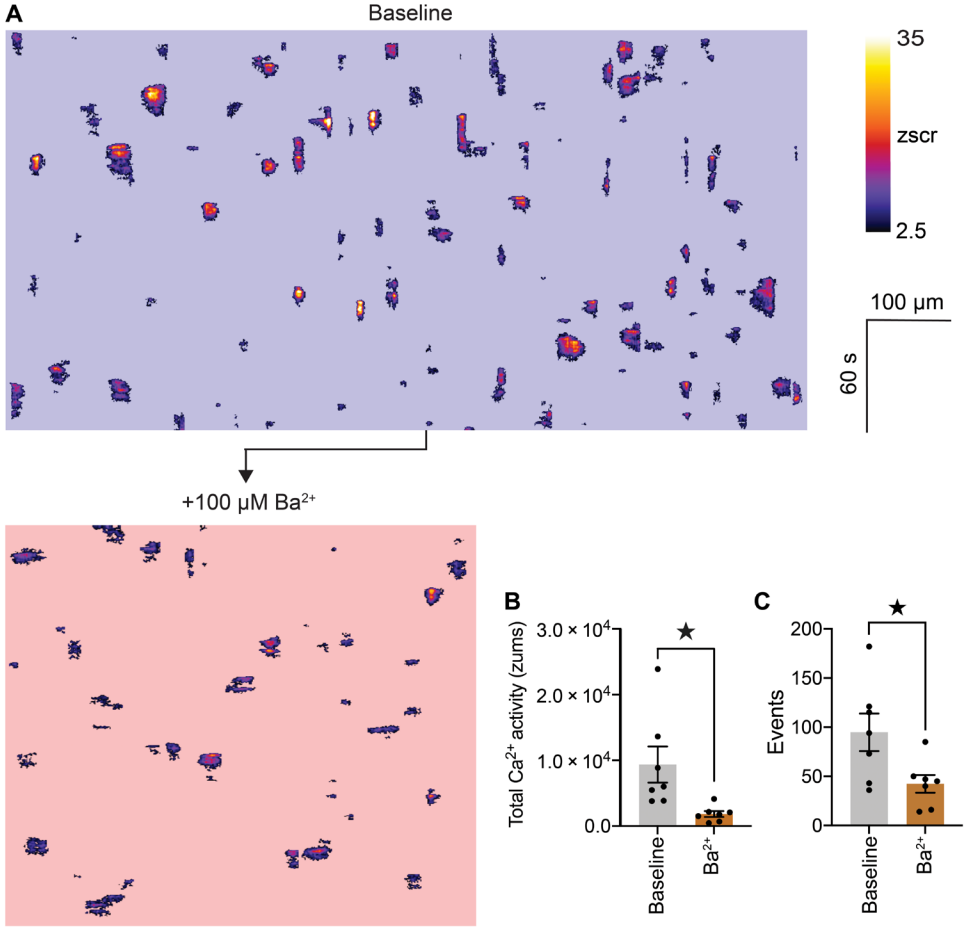

Fig. 4. Capillary Kir2.1 channel–mediated electrical signaling shapes Ca^{2+} signaling. (**A**) ST maps extracted from the same field before and after inhibition of Kir2.1 channels with topically applied Ba^{2+} (100 µM). (**B**) Summary data showing the in vivo effects of Ba^{2+} on total Ca^{2+} activity [n = 7 experiments, 7 mice; P = 0.0353 (t_6 = 2.706), paired Student's t test] and total number of events observed (**C**) [n = 7 experiments, 7 mice; P = 0.0401 (t_6 = 2.610), paired Student's t test].

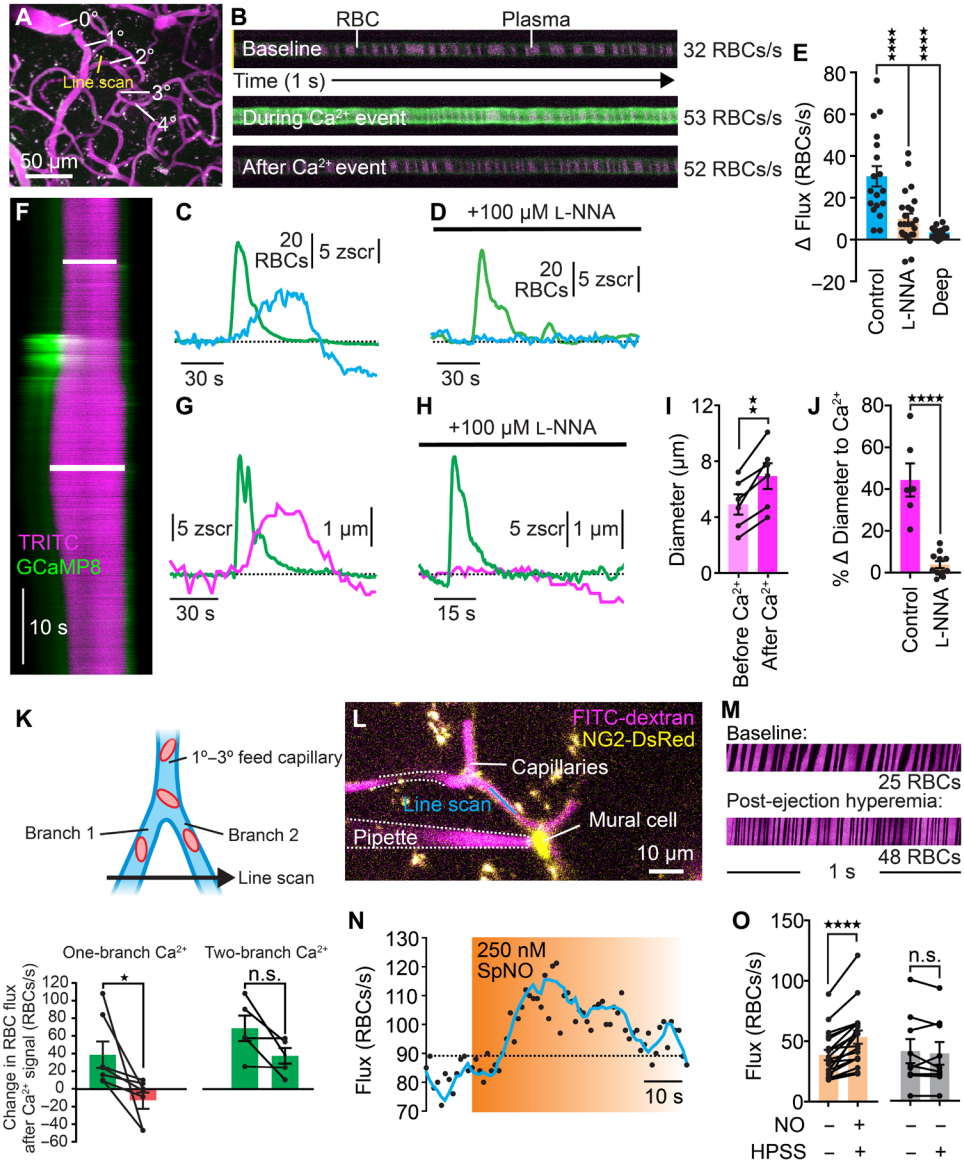

Fig. 5. Ca^{2+} signaling tunes capillary diameter and blood flow. (**A**) Flux experiment setup. (**B**) Line scans showing RBCs (black) passing through a capillary in fluorescent plasma (*x*, time; *y*, space). (**C**) Hyperemia (blue) following a spontaneous Ca^{2+} signal (green). (**D**) L-NNA inhibition of Ca^{2+}-associated increases in RBC flux. (**E**) Changes in flux after a Ca^{2+} event at 1° to 3° bifurcations of the capillary network with and without L-NNA and in deeper capillaries (≥5°) [$n = 18$ to 24 experiments, 7 to 9 mice; $P = 0.0001$ ($q_{58} = 4.768$) control versus L-NNA; $P = 0.0001$ ($q_{58} = 5.965$) control versus deep; one-way ANOVA and Dunnett's multiple comparison test]. (**F**) Line scan showing capillary dilation to a Ca^{2+} event (*y*, time; upper bar, baseline; lower bar, peak). (**G**) Diameter (magenta) and Ca^{2+} (green) for the experiment in (F). (**H**) As in (G), an experiment following cortex perfusion with L-NNA. (**I**) Dilation following Ca^{2+} signaling [$n = 6$ experiments, 5 mice; $P = 0.0029$ ($t_5 = 5.438$); paired *t* test]. (**J**) L-NNA inhibition of Ca^{2+}-induced dilation [$n = 6$ to 11 paired experiments, 5 to 7 mice; $P < 0.0001$ ($t_{15} = 6.589$); unpaired *t* test]. (**K**) Directional control of blood flow by capillary Ca^{2+}. Top: Experimental approach. Two branches, fed by a 1° to 3° capillary, were simultaneously line-scanned. Bottom: Summary showing differential blood flow when a Ca^{2+} signal occurred in one branch only (left) and uniform blood flow through the two segments when a signal occurred in both branches (right). [one-branch Ca^{2+} event: $n = 7$ paired experiments; $P = 0.0395$ ($t_6 = 2.621$); paired *t* test; two-branch Ca^{2+} event: $n = 5$ paired experiments; $P = 0.0837$ ($t_4 = 2.292$); paired *t* test]. (**L**) Pipette containing spermine NONOate next to a pericyte. Flux was measured by line-scanning the capillary during ejection. (**M**) RBCs passing through the line-scanned region against fluorescent plasma (*x*, time). (**N**) Time course of RBC flux to NO. (**O**) Peak RBC flux at baseline and after NO [$n = 19$ experiments, 8 mice; $P < 0.0001$ ($t_{18} = 5.714$); paired *t* test] or HPSS [$n = 9$ experiments, 5 mice; $P = 0.4587$ ($t_8 = 0.7784$); paired *t* test].

Ca^{2+} signals were detected in two daughter branches fed by the same higher-order capillary, blood flow measurements revealed a simultaneous increase in RBC flux in both daughter branches. Notably, however, if a Ca^{2+} signal was detected in only one branch, flux preferentially increased through that branch (Fig. 5K). This suggests that capillary Ca^{2+} events impart directional control of blood flow through the capillary bed, as previously reported by our group (*5*), favoring flux through branches in which Ca^{2+} events occur.

Given the contractile nature of pericytes in the initial segments of the capillary bed, we reasoned that the observed increases in blood flow reflected relaxation of these cells in response to the Ca^{2+}-dependent production of a diffusible factor by cECs. Accordingly, we focused our attention on NO, a potent vasodilator generated by

Ca^{2+}-dependent endothelial nitric oxide synthase (eNOS) with an established role in arteriolar EC–mediated vasodilation (*27*). To test for a possible contribution of NO in the capillary bed, we applied the NOS inhibitor L-NNA (100 μM) to the cranial surface and measured RBC flux in relation to cEC Ca^{2+} events. Application of L-NNA reduced the magnitude of RBC flux increases associated with capillary Ca^{2+} signals by 68% (Fig. 5, D and E), without substantially affecting the underlying Ca^{2+} signals (fig. S13). To further test the hypothesis that NO released by cECs causes relaxation of contractile pericytes, we determined whether capillary Ca^{2+} events are associated with local increases in capillary diameter. Consistent with this supposition, we found that these events routinely preceded dilations of affected first- to third-order capillary branches; notably, these dilations averaged 2.0 ± 0.4 μm (n = 6 experiments, 5 mice; Fig. 5, F, G, I, and J), a marked (~40%) increase relative to the basal diameter of these capillaries (4.9 ± 0.7 μm). Notably, these dilations were almost completely abolished by the NOS inhibitor L-NNA (100 μM), consistent with the interpretation that cEC-produced NO drives local pericyte relaxation (Fig. 5, H and J). Last, to directly test whether a local elevation of NO around capillary pericyte is capable of increasing blood flow, we maneuvered a pipette containing spermine NONOate (250 nM) into the brain of an NG2-DsRed mouse and positioned it adjacent to a pericyte located at a first- to third-order capillary branch point (Fig. 5L). Pressure ejection of this NO donor, but not the Hepes-buffered salt solution (HPSS) vehicle, directly onto a DsRed+ pericyte caused a marked (~46%) increase in RBC flux through the underlying capillary in 74% of trials (mean increase, 15 ± 3 RBCs/s; Fig. 5, M to O), consistent with cEC-derived NO causing pericyte relaxation. In contrast, pressure ejection of spermine NONOate onto capillaries lacking contractile pericytes (≥5th order) had no effect on RBC flux (fig. S14).

DISCUSSION

We previously demonstrated that capillaries communicate with penetrating arterioles by initiating long-range, rapid, hyperpolarizing signals that control arteriolar diameter and blood flow (*19*). Here, using in vivo Ca^{2+} imaging in conjunction with a newly developed image analysis technique, we reveal a previously unanticipated universe of dynamic Ca^{2+} signals in brain cECs that are notable for their diversity and longevity. These events, which reflect intracellular Ca^{2+} release through IP_3Rs in the ER, are driven by neuronal activity, mediated by G_qPCR signaling, and enhanced by Ca^{2+} entry through plasmalemmal TRPV4 channels. The amplitude, spread, and duration of capillary Ca^{2+} signals appear to be inextricably linked through CICR to form a hierarchy of Ca^{2+} signals, ranging from brief, low-amplitude protoevents to larger and longer unitary and compound events. Capillary Ca^{2+} events regulate branch-by-branch blood flow by communicating with local pericytes through generation of NO, directing capillary blood flow with great precision (fig. S15). The enormous range of active site durations (<1 to 56 s) and Ca^{2+} output (up to 10,000-fold difference) within an individual cEC suggests that the degree and extent of resultant NO production can be finely graded. Together with our prior work, these data suggest a model in which capillaries use both Ca^{2+} and electrical signaling to direct blood flow to active regions, such that capillary Ca^{2+} acts locally in the initial segments of the capillary bed over longer (up to a minute) time scales to direct local blood flow down specific branches via NO, and electrical signaling acts over the longer distances between capillaries and upstream arterioles to control blood flow at a macroscopic level and on a faster (millisecond) time scale (fig. S15).

cEC Ca^{2+} and electrical signaling: An integrated perspective

Intriguingly, our data strongly imply that these electrical and Ca^{2+} signaling modes within capillaries are intricately entwined, as blocking electrical signaling caused a marked reduction in capillary Ca^{2+} signaling. Thus, our results suggest that electrical signals act not only to dilate upstream arterioles but also to support and amplify Ca^{2+} entry in cECs. The membrane hyperpolarization provided by electrical signaling would increase Ca^{2+} influx across the plasmalemma through cEC TRPV4 channels. Functional TRPA1 channels have also been reported in cECs (*28*), and Ca^{2+}-permeable TRPC3, TRPM3, TRPP2, P2X4, P2X7, and Piezo1 channels have been detected at the mRNA level (*29*). Furthermore, IP_3R-mediated Ca^{2+} events lead to varying degrees of ER Ca^{2+} depletion, which would cause activation of store-operated Ca^{2+} entry (SOCE), the magnitude of which would be influenced by the driving force for Ca^{2+} entry. Consistent with this possibility, brain cECs express the SOCE channels Orai1 and Orai3 (*29*). Passing electrical signals are thus expected to "precondition" capillaries for Ca^{2+} entry, augmenting NO production in these electrically active vessels to promote pericyte relaxation and further enhance blood flow in the direction of active neurons. Further work is needed to fully understand the relationship between capillary electrical and Ca^{2+} signals and to map the full complement of Ca^{2+} entry pathways across the plasmalemma.

Capillary Ca^{2+} signals in a broader context

Considered in the macroscopic context of the endothelium, our data establish that Ca^{2+} signals in cECs are distinct from those that occur in arteriolar ECs and also exhibit unique properties compared with those in other vascular beds. In this latter context, our characterization of brain EC Ca^{2+} dynamics unexpectedly revealed that capillary events do not propagate to upstream arterioles or even between cells but rather remain localized within a single cEC. This was unexpected, given that, in cremaster arterioles, local application of a G_qPCR agonist evokes long-range Ca^{2+} events in ECs that propagate at a velocity in excess of 100 μm/s for up to ~1 mm (*30*). Such long-distance propagating Ca^{2+} signals would require a mechanism for intercellular IP_3 regeneration that does not appear to be in play in brain capillaries. Instead, our data show that Ca^{2+} spreads within an individual EC, possibly through Ca^{2+}-dependent activation of adjacent IP_3Rs and TRPV4 channels, strongly supporting a local signaling function.

A growing body of evidence has established that 1st- to ~4th-order capillaries, which are covered by contractile pericytes, dilate during functional hyperemic responses and are critical for blood flow control in the brain (*10*, *24*). Our data now provide a mechanistic basis for the local control of the diameter of these branches and further suggest multiple roles for capillary Ca^{2+} signals in different contexts and locations. Our data show that during functional hyperemia, when hundreds of thousands of local neurons act in concert (*31*), Ca^{2+} is rapidly and robustly elevated simultaneously in ECs throughout first- to third-order capillaries, dilating these branches to promote a substantial increase in blood flow. This broad Ca^{2+} elevation through multiple branches supports the wide distribution of blood necessary to support the metabolic demands of many neurons distributed across a large territory of the cortex. We also observed Ca^{2+} elevations occurring asynchronously in single cells. These events,

presumably reflecting responses to the activity of a very small number of neurons, locally dilate individual first- to third-order vessels. This mode of Ca^{2+} signaling thus provides a mechanism for exquisite fine-tuning of local blood flow, thereby optimizing energy substrate supply to highly localized demand. Although it was recently reported that optogenetic stimulation of pericytes at fifth-order and above capillaries induces slow contractions that regulate capillary diameter and blood flow (*32*), we found that ambient Ca^{2+} events in these deeper capillaries had no detectable effect on blood flow or diameter, suggesting that Ca^{2+} events here have roles beyond blood flow control.

How many channels are recruited during the smallest capillary Ca^{2+} events?

In comparing our data with previously published reports, we noted that protoevents closely resemble previously reported single IP_3R release events referred to as Ca^{2+} "blips" (*33*), which our analyses (based on data reported in this latter study) show have a site diameter of 1.6 ± 0.2 μm and estimated duration of 1.0 to 1.8 s (five observations). Typically reported Ca^{2+} blip amplitudes, converted to zscr, ranged from 3.0 to 6.0 (median, 4.4; 15 observations). Notably, our data show that in vivo recorded cEC protoevents with similar active site diameters (≤1.6 μm; n = 92 observations, 34 mice) had amplitudes of 3.0 to 8.0 zscr (median, 4.8 zscr) and durations of 1.2 to 3.6 s (median, 2.0 s). These similarities in the ST characteristics of blips (*33*) and cEC protoevents are consistent with the possibility that protoevents reflect Ca^{2+} release from a single IP_3R channel.

Further roles for capillary Ca^{2+} elevations

In the in vivo milieu, cECs are exposed to a range of physical forces (e.g., fluid shear forces, physical contact with passing erythrocytes, and paravascular flow through the glymphatic system) (*34*), chemical modulators [e.g., neurovascular coupling (NVC) agents released by neurons and astrocytes and fluctuating pO_2, pCO_2, and pH], and electrical influences (K_{IR} channel–mediated propagating hyperpolarization) (*19*) that shape their signaling behavior. Ca^{2+} elevation is the nexus for an enormous range of cellular functions; thus, Ca^{2+} events in cECs are expected to perform functions beyond the generation of NO and control of blood flow. Ca^{2+} events may be coded to a particular function through their ST patterning (e.g., spatial spread, subcellular localization, amplitude, or frequency) and could take on different properties and have different roles depending on the nature of surrounding neuroglial activity. Possible alternative functions include Ca^{2+}-dependent control of blood-brain barrier tightness (*35*), modulation of gene expression (*36*), and generation of other paracrine signaling molecules. Another possibility is that release of NO into the vessel lumen could stimulate oxygen displacement from transiting RBCs (*37*) and could plausibly contribute to upstream arteriolar dilation, provided that the distance from the capillary to the arteriolar wall is sufficiently short (*38*).

Matching local blood flow to neuronal activity: How precise is precise enough?

An implicit question in studies of dynamic regulation of blood flow in the brain is how granular are the NVC mechanisms that match neuronal energy requirements to changes in blood flow. Put another way: How many active neurons does it take to cause a significant increase in blood flow, and how small of a territory can this increment in blood flow be targeted to? Studies performed using brain slices suggest that activation of a single neuron is sufficient to evoke an arteriolar response (*39*), although the functional linkages among different cell types that might be necessary to produce this response have not been elucidated. In any case, without a mechanism for locally controlling blood distribution, for example, through coordinated capillary Ca^{2+} signaling, the flow of incoming blood triggered by neuronal activity could needlessly overperfuse relatively quiescent neurons within its perfusion domain (*19*). Our data strongly suggest that a finer degree of regulation at branch points deeper in the capillary bed greatly increases the resolution of blood flow control and directs RBCs to smaller populations of neurons.

MATERIALS AND METHODS

Generation of *Cdh5*^{BAC}-GCaMP8 mice

The BAC clone RP23-453P1, containing 124 kb of 5′ and 33 kb of 3′ DNA flanking the *Cdh5* (cadherin 5) locus, was obtained from the Children's Hospital Oakland Research Institute. The GCaMP8-poly(A) cassette was inserted at the start codon of the *Cdh5* coding sequence in exon 2 by homologous recombination using a targeting vector designed for BAC recombineering in SW105 *Escherichia coli*, as previously described (*4*). *Cdh5*^{BAC}-GCaMP8-poly(A) DNA was prepared using a modified alkaline lysis protocol (NucleoBond BAC 100 Kit), and PI–Sce I linearized DNA was microinjected into fertilized embryos using standard pronuclear injection techniques. Founders were identified by polymerase chain reaction amplification of GCaMP sequences using the forward and reverse primers calmF (5′-AAG GGC GAG GAG CTG TTC A-3′) and calmR (5′-CGA TCT GCT CTT CAG TCA GTT GGT-3′), respectively, and back-crossed to C57/BL6J mice for six generations (B6.N6). Mice were phenotyped, and the functional activity of the genetically encoded indicator GCaMP8 was verified by immunolocalization of GCaMP8 protein and detection of EC Ca^{2+} signaling. All procedures were approved by the Cornell Institutional Animal Care and Use Committees and adhered to standards published in the *Guide for the Care and Use of Laboratory Animals*.

Animal husbandry

Adult (2- to 3-month-old) male and female C57BL6 mice, *Cdh5*^{BAC}-GCaMP8 mice, and NG2-DsRed mice (C57/BL6J background; Jackson Laboratories) were group-housed on a 12-hour light:dark cycle with environmental enrichment and free access to food and water. All animal procedures received prior approval from the University of Vermont Institutional Animal Care and Use Committee.

Chemicals

Tetrodotoxin citrate, CPA, and PGE_2 were obtained from Tocris Bioscience, and ethyleneglycol-bis(β-aminoethyl)-*N*,*N*,*N*′,*N*′-tetraacetoxymethyl ester (EGTA-AM) was obtained from EMD Millipore. Alexa-633 hydrazide was obtained from Thermo Fisher Scientific. FR900359, purified from a dried leaf extract of *Ardisia crenata* as described previously (*15*), was provided by E.K. and G.M.K. (University of Bonn, Germany). Unless otherwise noted, all other chemicals were obtained from Sigma-Aldrich.

In vivo imaging resolution and validation

The lateral resolution of our imaging system, measured using an Invitrogen PS-Speck microscope point source kit and the Metroloj Fiji plugin, was 328 nm. The practical *xy* resolution limit of objects that could be reliably thresholded as discrete entities—after accounting for field of view (FOV) degradation at depth, pixel representation at

20×, and noise reduction routines (see below)—was ~5 pixels by 5 pixels, corresponding to a radius of 2.3 μm. This level of resolution was extremely conservative to minimize the chance of including random "shot noise" clumps (see below). For subsequent extraction of temporal information using the ST map approach, averaging perpendicularly across capillaries increased the signal-to-noise ratio, allowing a lateral spatial resolution of 1.6 μm. Imaging GCaMP8 at 800 nm, a wavelength at which Ca^{2+} binding–evoked fluorescence changes are undetectable, revealed no changes in the signal that would indicate artifactual contributions from small *xyz* motions of the sample.

Acute brain slices

Endothelium and nuclei were stained by delivering Di-8-ANEPPS (25 μM; Invitrogen) and Hoechst 33342 (150 μM; Tocris) into C57/BL6J mice via transcardiac perfusion. Slices were prepared essentially as previously described (*40*). Briefly, the brain was rapidly removed into ice-cold aCSF (124 mM NaCl, 3 mM KCl, 2 mM $CaCl_2$, 2 mM $MgCl_2$, 1.25 mM sodium phosphate buffer, 26 mM $NaHCO_3$, and 4 mM glucose). Slices (160 μm thick) were prepared using a Leica VT 1000S vibratome and stored in oxygenated aCSF. Brain slices were imaged using two-photon laser scanning microscopy, as described above, with continuous perfusion of oxygenated (20% O_2 and 5% CO_2) aCSF.

Surgery

Mice were anesthetized with isoflurane (5% induction and 2% maintenance). Upon obtaining surgical-plane anesthesia, the skull was exposed, and a stainless steel head plate was attached over the left hemisphere using a mixture of dental cement and superglue. The head plate was secured in a holding frame, and a ~2-mm-diameter circular cranial window was drilled in the skull above the somatosensory cortex (approximately −1.5 mm anteroposterior, 3.0 mm mediolateral versus bregma). A solution of 3 mg/ml (150 μl) of TRITC-dextran (molecular weight, 150 kDa) in saline was systemically administered via retro-orbital injection to enable subsequent visualization of the cerebral vasculature and contrast imaging of RBCs. Upon conclusion of surgery, isoflurane anesthesia was replaced with α-chloralose (50 mg/kg) and urethane (750 mg/kg).

In vivo imaging

Body temperature was maintained at 37°C throughout the experiment using an electric heating pad. aCSF was applied to the exposed cortex for the duration of the experiment. Single-plane imaging experiments involved imaging a 424 μm–by–424 μm field at ~2.5 Hz for 236 s. A typical 4D imaging experiment assessed a field of the same *xy* dimensions, plus ~50 μm in the *z* axis (2 μm spacing between planes), creating 90 3D volumes over ~20 min. RBC flux was measured by performing line scans at 15 kHz. In experiments using simultaneous measurement of RBC flux and Ca^{2+} signals, line scans were oriented perpendicular to the vessel and stretched a short distance into the surrounding parenchyma. When measuring blood flow alone, the line scan was oriented along the lumen parallel to the flow of blood, which improves flux signal. For pressure ejection of agents in aCSF (vehicle) onto capillaries, a pipette containing the agent and TRITC-dextran or FITC-dextran (to enable visualization) was maneuvered into the cortex and positioned adjacent to the capillary under study, after which the solution was ejected directly onto the capillary (4 to 10 psi, 300 ms). This approach restricted agent delivery to the target capillary and caused minimal displacement of the surrounding tissue. For pharmacological and staining experiments, agents of interest were applied to the cranial surface for a minimum of 30 min to allow penetration. The exception was Alexa-633 hydrazide (2 mg/kg), which was delivered into the bloodstream via the retro-orbital sinus. Electrical FPS (4-s square train, 5-ms pulse width, 10 Hz, 0.4 to 0.9 A) was delivered to the contralateral forepaw through a pair of 30-G needles inserted beneath the skin. Images were acquired through a Zeiss 20× Plan Apochromat 1.0 NA DIC VIS-IR water-immersion objective mounted on an LSM-7 microscope (Zeiss) coupled to a Coherent Chameleon Vision II Titanium-Sapphire pulsed infrared laser (Coherent). GCaMP8 and TRITC-dextran were excited at 920 nm, and emitted fluorescence was separated through 500- to 550- and 570- to 610-nm bandpass filters, respectively.

Immunohistochemistry and native fluorescence

Tissues were fixed in 4% paraformaldehyde overnight at 2° to 8°C and dehydrated in 30% sucrose in 1× phosphate-buffered saline (PBS) before embedding. For recording native fluorescence of GCaMP8 molecules, 8-μm cryosections were mounted with Vectashield (Vector Laboratories) and imaged using a Leica DMI6000B inverted microscope equipped with a QImaging Retiga 2000R digital camera. For anti-GFP (green fluorescent protein) immunohistochemistry, cryosections were rinsed in PBS containing 0.01% Tween 20 before heat-induced antigen retrieval [10 mM citrate buffer (pH 6.0)]. Endogenous peroxidase activity was quenched with 3% hydrogen peroxide in methanol, and nonspecific binding was blocked with normal goat serum (Vector Laboratories). Blocked sections were incubated overnight at 2° to 8°C with rabbit anti-GFP polyclonal antibody (1/500 dilution, sc-8334; Santa Cruz Biotechnology) and developed with biotinylated goat anti-rabbit secondary antibody/horseradish peroxidase–conjugated streptavidin/AEC reagent. Slides were counterstained with hematoxylin, mounted with Fluoromount-G, and digitally scanned on a Leica Biosystems Aperio CS2 digital pathology scanner. Sections from nontransgenic littermates, in which no staining was observed, were imaged as negative controls.

Data analysis

Data preparation

Image stacks (.lsm format: *xy* dimensions = 512 pixels by 512 pixels, 425 μm by 425 μm) were imported into ImageJ (ImageJ64 1.48v, W. Rasband, National Institutes of Health) using the Bio-Formats Importer plugin. Red (TRITC-dextran) and green (GCaMP8) color channels were separated and saved as independent multistack TIFFs and then calibrated for planar (*xy*) pixel dimension, slice spacing (depth: *z* pixel dimension), and plane acquisition time (time: *t* temporal dimension). Single-channel multistack TIFFs were opened in custom-written software (VolumetryG9; G.W.H.).

Novel approaches for quantifying Ca^{2+} fluorescence

Reliably and consistently extracting fluorescence intensities from active areas requires demarcation of the exact spatial area of each active site. This prevents nonvessel background from being averaged into the fluorescent signal [a common problem when using rectangular regions of interest (ROIs) on irregularly shaped objects], thereby providing a more realistic and accurate measurement of the actual magnitude of Ca^{2+} signals. Existing methodologies, such as F/F_0 or F/F_{avg}, background subtraction and differentiation (dI/dT), have limitations due to the wide array of basal fluorescence intensities present in vessels expressing GCaMP8 (fig. S4). Bright objects have larger variations in intensity due to shot noise that remains regardless of the type of amplitude intensity manipulations and corrections

used. Attempts to threshold Ca^{2+} signals from vessels with low basal fluorescence invariably encounter background noise from vessels with higher basal fluorescence. To resolve this issue, we applied a number of signal-to-noise and statistical techniques to fluorescence imaging, notably including imaging decibels and *z* scores. At its core, this main approach is based on variations in fluorescence intensity, not absolute intensity levels. Two variations of this technique were used to (i) demarcate the spatial areas of Ca^{2+} events and (ii) quantify fluorescence intensity from ST maps using a standardized fluorescence intensity unit (*z* score: zscr).

Image processing overview

The analysis of Ca^{2+} events in capillaries involves a number of steps designed to reduce user input by leveraging statistical definitions of dynamic Ca^{2+} objects in both space and time. The development of this analysis has resulted in new terms and acronyms:

1) Active site: Statistically defined, contiguous spatial region in which elevated Ca^{2+} levels were detected.

2) idB: Imaging decibel. A logarithmic unit of intensity useful in large dynamic range (16- to 32-bit) imaging.

3) Multithreshold: Thresholding multiple specific intensity bands.

4) PTCL: Coordinate-based "particle" (or object).

5) RIBN: ST map containing multiple elements or "ribbons."

6) zscr: Statistical *z* score. Relates a value to the SD of the sample.

The workflow for single-plane Ca^{2+} images is divided into four main sections: (i) movie preprocessing, (ii) active site discrimination, (iii) active site masking, and (iv) ST map construction and PTCL analysis. These are described in detail below and are depicted in fig. S3.

Movie preprocessing. Raw movie files typically suffer from scanning misalignment artifacts (referred to as "combing") and frame-to-frame noise. The following steps were taken to improve the clarity and resolution of static and dynamic objects in the FOV. Steps (a) and (f) were always applied; the remaining steps were used where appropriate.

Artifact type	Correction
(a) Combing	Apply even-row horizontal offset in combination with left- and right-side scaling.
(b) Bleaching	Plot time course of intensity in nonvessel region. Calculate decay slope and apply correction to movie frames.
(c) Flickering	Plot time course of intensity in nonvessel region and assess for abrupt changes in intensity. Apply correction by adding/subtracting frame intensity to the baseline average.
(d) Motion (*xy* axes)	Select nondynamically fluorescing objects and track *xy* position using the difference algorithm. Motion-stabilize movie by applying inverse tracking coordinates and offsetting movie frame.
(e) Motion (*z* axis)	Crop out large *z*-motion bumps that change the depth of the imaging plane, leaving a contiguous section that preserves the same depth plane.
(f) Noise	Apply ±1 frame average (3 frames) followed by Gaussian blur (3 × 3 pixels; SD = 1.0)

Examples of imaging preprocessing are provided in fig. S3 (A to E).

Active site discrimination. The structural identification of capillaries from background GCaMP fluorescence and plasma contrast (TRITC) is often problematic due to the "shadowing" effect of large overlying pial vessels, orientation issues (i.e., vessels angled in the *z* axis), and changes in blood flow rates that affect TRITC fluorescence. An alternative, more efficient approach is to use Ca^{2+} events in vessels to demarcate the vessel segments owing to their better dynamic signal-to-noise ratios. The following process was optimized for capillary Ca^{2+} events, which are infrequent, discrete, and separated by periods in which Ca^{2+} levels return to a consistent, stable baseline. The main statistical principle on which this analysis is based is that a Ca^{2+} event occurring during a particular span of time will increase the overall SD of intensity values in that time span. Subsequent differentiation of SD values is extremely effective in demarcating where an active (or decaying) Ca^{2+} transient is occurring.

Procedure	Description
(a) Calculating SD	Divide movie into a series of time spans and calculate temporal SD in each time span for every pixel in the FOV. Typical time spans were 10.6 to 12.2 s (27 to 31 frames).
(b) Differential SD (idB)	Subtract each time span SD from that of the previous time span (+offset) and convert to idB (see Eq. 1) (*41*,*42*).
(c) Multithresholding	Select and remove differential SD intensities greater than +3.7 idB and less than −3.7 idB.
(d) Filtering noise particles	Gauss 3 × 3 filter and then filter out small shot noise particles in intensity range (<25 pixels)
(e) Converting to coordinates	Convert each contiguous thresholded area to coordinate-based objects and save.

Examples of active site discrimination are provided in fig. S3 (F to I).

Active site masking. The processing described above returns consistent, statistically defined, dynamic Ca^{2+} areas in capillaries that are used to mask active sites and quantify intensity changes associated with Ca^{2+} events. This section requires a user decision (leave or remove) to determine which objects will remain in the analysis.

Procedure	Description
(a) Prevalence map creation	Sum the positions of coordinate-based objects for each time span to generate a prevalence map that is color-coded according to how many time spans in which an object was active.
(b) Feature refinement	Erase unwanted vascular structures (arterioles) or small noise artifacts (brightness, motion, etc.).
(c) Branch splitting	In cases where all parts of a branch structure are active, separate branches into linear segments.
(d) Active site mask	Save the refined prevalence map as a particular type of mask (e.g., capillary active site mask).
(e) ROI bitmasks	Convert contiguous active sites in the mask to ROIs, with bounding rectangles and a bitmask representing the area of the capillary defined as an active site.

Examples of active site masking are provided in fig. S3 (J and K).

ST map construction and PTCL analysis. The final part of the processing uses ST maps to summarize Ca^{2+} activity in all defined active masks. Ca^{2+} events in ST (RIBN) maps are statistically demarcated and filtered using a two-part process developed for this purpose involving estimating the variation during quiescent background periods followed by thresholding. All analyses are extracted from ST (RIBN) maps.

Procedure	Description
(a) Guide angle	Calculate the orientation angle of the active site using a fast quadrant bias method in combination with major and minor side lengths. Quadrant biases <66% result in orthogonal guides.
(b) Perpendicular rays	Create a coordinate list of perpendicular points from the guide to the bounding rectangle for every point along the guide. Angled guide length corresponds to the Pythagorean distance across the rectangle.
(c) Circumferential averaging	Sum pixel intensities along each perpendicular ray within the active site mask to generate a single average pixel intensity at that point along the guide.
(d) Creation of RIBN ST map	Transfer the line of average circumferential pixel intensities along the guide to an ST map, with distance along the guide indicated in the horizontal axis and lines from each frame of the movie stacked vertically (top, start of video; bottom, end of video). The above processes are repeated for every defined active site in the FOV.
(e) Conversion to zscr (SDq)	Assess fluctuations of intensity during quiescent background periods by estimating the percentage of time each active site was inactive (35% used). Then, create a histogram of values for each pixel column and calculate the SD of the dimmest 35% of values. This SD(minima) is used to demarcate quiescent regions in each pixel column [≥10×SD(minima)]. SD is recalculated in each quiescent region from original intensity values to generate both the quiescence average intensity and quiescence SD (SDq). Each pixel column is converted to a *z* score (zscr), and values less than 2.5×SDq are discarded.
(f) Overall Ca^{2+} output	Calculate the overall Ca^{2+} activity generated by all active sites in capillaries in the FOV by summing all zscr pixels in the zscr (RIBN) map and normalizing the activity per minute. Each map pixel represents 0.83 μm and 0.39 s (0.326 μm·s), which is multiplied by the zscr intensity. The integrated Ca^{2+} output has units of zscr·μm·s min^{-1}, abbreviated zums.
(g) Ca^{2+} event analysis	Convert each contiguous ST Ca^{2+} event to a coordinate-based PTCL format that enables more efficient shape analysis. Then, calculate the overall duration (s) and longitudinal length (width: μm), as well as the location of maxima and rise and decay characteristics. Outer perimeters enable determination of leading-edge velocities, and intervals between Ca^{2+} events enable calculation of the occurrence of Ca^{2+} events.

Examples of active site masking are provided in fig. S3 (L to Q). Further details of the analysis process are provided below. See movie S11

$$\mathrm{idB}_{\sigma} = \log_{10}\left(\frac{\sigma_{(n)}}{\sigma_{(n-1)}}\right) \cdot 20 \quad (1)$$

$$\mathrm{zscr} = \frac{\mathrm{Intensity} - \mathrm{AVG_q}}{\mathrm{SD_q}} \quad (2)$$

Quantification of capillary RBC flux

Because repetitive single-line scan images are similar to ST maps, plasma signals were analyzed using PTCL analysis (see above). To quantify RBC flux and velocity (where appropriate), we calculated the diameter, leading and trailing slopes, and intervals between PTCLs (created from plasma signals between RBC shadows). A secondary measure of RBC flux was obtained using an algorithm that detects transient dimming in the TRITC-dextran or FITC-dextran signal associated with passing RBCs using SparkAn (A. Bonev). Positive events were binned at 1-s intervals to provide a measure of RBC flux. Occasional inappropriately flagged events were rejected by the analyst. At very high fluxes (>100 RBCs/s), cells could follow one another so closely as to appear as one event (fig. S16); in these instances, flux may be underestimated. To quantify baseline versus NO-induced RBC flux, we compared maximum flux values during the baseline recording period before NO-donor delivery to the peak flux during the period after NO delivery.

4D volume imaging

4D recording comprises a temporal sequence of volumes, with each volume created by scanning multiple slices through the depth of the mouse somatosensory cortex. Structural volume scans measuring 425 μm by 425 μm to 607 μm by 607 μm in the *xy* axes were performed to an average *z* depth of 240 ± 20 μm (1-μm *z* steps) from the pial vessel border for 7 to 22 min. Volumes were decombed (see above), averaged (±1 μm), and smoothed (Gaussian blur, 3 × 3; SD = 1.0), and slice-based PTCLs of Ca^{2+} events in the angioarchitecture were created. To create 3D objects from Ca^{2+} events that occupied multiple subslices within a single volume (3D structure) or across multiple blocks (4D ST objects), we wrote a series of routines that efficiently calculated spatial and temporal overlap of PTCLs. These routines used PTCL bounds to pre-sort likely candidates followed by application of exact coordinate overlap functions. Once the within-volume (spatial depth overlap) was determined, the resulting 3D objects were projected into adjacent volumes to determine their temporal extent. A structural model of the angioarchitecture of blood vessels using TRITC-dextran fluorescence was also created. The percentage of the capillary network that displayed one or more Ca^{2+} transients was calculated by first summing all Ca^{2+} transient objects in the volume sequence as a single 3D volume and then determining the overlap of those 3D objects with the 3D blood vessel model. The distance between capillary branch points in layers 1 to 3 of the somatosensory cortex was measured by implementing a 3D flood-fill routine from a reference seed point and then calculating and mapping the distance of each voxel in each vessel network object to the seed point. At junctions, the intraluminal volume relative to the prejunctional vessel increases, allowing branch points in addition to vessel size characteristics to be identified. To check the accuracy of this technique, we manually verified all branch points. The distance of every voxel in Ca^{2+} event objects was compared to

the geometric center of identified branch points. The overall density of blood vessels and distance of parenchymal volume to the closest blood vessel were mapped and quantified using 3D Euclidian distance maps.

Statistics

Statistical testing was performed using GraphPad Prism 7 software. Data are expressed as means ± SEM, and a P value of ≤ 0.05 was considered significant. Stars denote significant differences; "n.s." indicates nonsignificant comparisons. Statistical tests are noted in the figure legends. All t tests were two-sided. Sample size was estimated on the basis of similar experiments performed previously in our laboratory (no statistical methods were used to predetermine sample sizes). Experiments were repeated to adequately reduce confidence intervals and avoid errors in statistical testing. Data collection was not performed blinded to the conditions of the experiments. Littermates were randomly assigned to experimental groups; no further randomization was performed. No data were excluded.

SUPPLEMENTARY MATERIALS

Supplementary material for this article is available at http://advances.sciencemag.org/cgi/content/full/7/30/eabh0101/DC1

View/request a protocol for this paper from *Bio-protocol*.

REFERENCES AND NOTES

1. R. Palmer, A. Ferrige, S. Moncada, Nitric oxide release accounts for the biological activity of endothelium-derived relaxing factor. *Nature* **327**, 524–526 (1987).
2. J. Ledoux, M. S. Taylor, A. D. Bonev, R. M. Hannah, V. Solodushko, B. Shui, Y. Tallini, M. I. Kotlikoff, M. T. Nelson, Functional architecture of inositol 1, 4, 5-trisphosphate signaling in restricted spaces of myoendothelial projections. *Proc. Natl. Acad. Sci. U.S.A.* **105**, 9627–9632 (2008).
3. S. K. Sonkusare, A. D. Bonev, J. Ledoux, W. Liedtke, M. I. Kotlikoff, T. J. Heppner, D. C. Hill-Eubanks, M. T. Nelson, Elementary Ca^{2+} signals through endothelial TRPV4 channels regulate vascular function. *Science* **336**, 597–601 (2012).
4. Z. Shen, Z. Lu, P. Y. Chhatbar, P. O'Herron, P. Kara, An artery-specific fluorescent dye for studying neurovascular coupling. *Nat. Methods* **9**, 273–276 (2012).
5. A. L. Gonzales, N. R. Klug, A. Moshkforoush, J. C. Lee, F. K. Lee, B. Shui, N. M. Tsoukias, M. I. Kotlikoff, D. Hill-Eubanks, M. T. Nelson, Contractile pericytes determine the direction of blood flow at capillary junctions. *Proc. Natl. Acad. Sci. U.S.A.* **117**, 27022–27033 (2020).
6. J. Ratelade, N. R. Klug, D. Lombardi, M. K. S. C. Angelim, F. Dabertrand, V. Domenga-Denier, R. A. S. Salman, C. Smith, J. F. Gerbeau, M. T. Nelson, A. Joutel, Reducing hypermuscularization of the transitional segment between arterioles and capillaries protects against spontaneous intracerebral hemorrhage. *Circulation* **141**, 2078–2094 (2020).
7. R. I. Grant, D. A. Hartmann, R. G. Underly, A.-A. Berthiaume, N. R. Bhat, A. Y. Shih, Organizational hierarchy and structural diversity of microvascular pericytes in adult mouse cortex. *J. Cereb. Blood Flow Metab.* **39**, 411–425 (2017).
8. J. Grutzendler, M. Nedergaard, Cellular control of brain capillary blood flow: In vivo imaging veritas. *Trends Neurosci.* **42**, 528–536 (2019).
9. R. A. Hill, L. Tong, P. Yuan, S. Murikinati, S. Gupta, J. Grutzendler, Regional blood flow in the normal and ischemic brain is controlled by arteriolar smooth muscle cell contractility and not by capillary pericytes. *Neuron* **87**, 95–110 (2015).
10. C. N. Hall, C. Reynell, B. Gesslein, N. B. Hamilton, A. Mishra, B. A. Sutherland, F. M. O'Farrell, A. M. Buchan, M. Lauritzen, D. Attwell, Capillary pericytes regulate cerebral blood flow in health and disease. *Nature* **508**, 55–60 (2014).
11. D. A. Hartmann, R. G. Underly, R. I. Grant, A. N. Watson, V. Lindner, A. Y. Shih, Pericyte structure and distribution in the cerebral cortex revealed by high-resolution imaging of transgenic mice. *Neurophotonics* **2**, 041402 (2015).
12. M. D. Sweeney, S. Ayyadurai, B. V. Zlokovic, Pericytes of the neurovascular unit: Key functions and signaling pathways. *Nat. Neurosci.* **19**, 771–783 (2016).
13. Y. N. Tallini, B. Shui, K. S. Greene, K. Y. Deng, R. Doran, P. J. Fisher, W. Zipfel, M. I. Kotlikoff, BAC transgenic mice express enhanced green fluorescent protein in central and peripheral cholinergic neurons. *Physiol. Genomics* **27**, 391–397 (2006).
14. I. G. Gould, P. Tsai, D. Kleinfeld, A. Linninger, The capillary bed offers the largest hemodynamic resistance to the cortical blood supply. *J. Cereb. Blood Flow Metab.* **37**, 52–68 (2016).
15. R. Schrage, A. L. Schmitz, E. Gaffal, S. Annala, S. Kehraus, D. Wenzel, K. M. Büllesbach, T. Bald, A. Inoue, Y. Shinjo, S. Galandrin, N. Shridhar, M. Hesse, M. Grundmann, N. Merten, T. H. Charpentier, M. Martz, A. J. Butcher, T. Slodczyk, S. Armando, M. Effern, Y. Namkung, L. Jenkins, V. Horn, A. Stößel, H. Dargatz, D. Tietze, D. Imhof, C. Galés, C. Drewke, C. E. Müller, M. Hölzel, G. Milligan, A. B. Tobin, J. Gomeza, H. G. Dohlman, J. Sondek, T. K. Harden, M. Bouvier, S. A. Laporte, J. Aoki, B. K. Fleischmann, K. Mohr, G. M. König, T. Tüting, E. Kostenis, The experimental power of FR900359 to study G_q-regulated biological processes. *Nat. Commun.* **6**, 10156 (2015).
16. A. Lacroix, X. Toussay, E. Anenberg, C. Lecrux, N. Ferreiros, A. Karagiannis, F. Plaisier, P. Chausson, F. Jarlier, S. A. Burgess, E. M. C. Hillman, I. Tegeder, T. H. Murphy, E. Hamel, B. Cauli, COX-2–derived prostaglandin E_2 produced by pyramidal neurons contributes to neurovascular coupling in the rodent cerebral cortex. *J. Neurosci.* **35**, 11791–11810 (2015).
17. M. J. Berridge, The inositol trisphosphate/calcium signaling pathway in health and disease. *Physiol. Rev.* **96**, 1261–1296 (2016).
18. O. F. Harraz, T. A. Longden, D. Hill-Eubanks, M. T. Nelson, PIP_2 depletion promotes TRPV4 channel activity in mouse brain capillary endothelial cells. *eLife* **7**, e38689 (2018).
19. T. A. Longden, F. Dabertrand, M. Koide, A. L. Gonzales, N. R. Tykocki, J. E. Brayden, D. Hill-Eubanks, M. T. Nelson, Capillary K^+-sensing initiates retrograde hyperpolarization to increase local cerebral blood flow. *Nat. Neurosci.* **20**, 717–726 (2017).
20. H. S. Silva, A. Kapela, N. M. Tsoukias, A mathematical model of plasma membrane electrophysiology and calcium dynamics in vascular endothelial cells. *Am. J. Phys. Cell Physiol.* **293**, C277–C293 (2007).
21. A. Y. Shih, P. Blinder, P. S. Tsai, B. Friedman, G. Stanley, P. D. Lyden, D. Kleinfeld, The smallest stroke: Occlusion of one penetrating vessel leads to infarction and a cognitive deficit. *Nat. Neurosci.* **16**, 55–63 (2012).
22. A. Schüz, G. Palm, Density of neurons and synapses in the cerebral cortex of the mouse. *J. Comp. Neurol.* **286**, 442–455 (1989).
23. S. Grubb, C. Cai, B. O. Hald, L. Khennouf, R. P. Murmu, A. G. K. Jensen, J. Fordsmann, S. Zambach, M. Lauritzen, Precapillary sphincters maintain perfusion in the cerebral cortex. *Nat. Commun.* **11**, 395 (2020).
24. R. L. Rungta, E. Chaigneau, B.-F. Osmanski, S. Charpak, Vascular compartmentalization of functional hyperemia from the synapse to the pia. *Neuron* **99**, 362–375.e4 (2018).
25. D. C. Hill-Eubanks, M. E. Werner, T. J. Heppner, M. T. Nelson, Calcium signaling in smooth muscle. *Cold Spring Harb. Perspect. Biol.* **3**, a004549 (2011).
26. M. S. Taylor, M. Francis, Decoding dynamic Ca^{2+} signaling in the vascular endothelium. *Front. Physiol.* **5**, 447 (2014).
27. S. Moncada, A. Higgs, The L-arginine-nitric oxide pathway. *N. Engl. J. Med.* **329**, 2002–2012 (1993).
28. P. Thakore, M. G. Alvarado, S. Ali, A. Mughal, P. W. Pires, E. Yamasaki, H. A. Pritchard, B. E. Isakson, C. H. T. Tran, S. Earley, Brain endothelial cell TRPA1 channels initiate neurovascular coupling. *eLife* **10**, e63040 (2021).
29. D. C. G. Garcia, T. A. Longden, Ion channels in capillary endothelium. *Curr. Top. Membr.* **85**, 261–300 (2020).
30. Y. N. Tallini, J. F. Brekke, B. Shui, R. Doran, S. M. Hwang, J. Nakai, G. Salama, S. S. Segal, M. I. Kotlikoff, Propagated endothelial Ca^{2+} waves and arteriolar dilation in vivo: Measurements in Cx40BAC GCaMP2 transgenic mice. *Circ. Res.* **101**, 1300–1309 (2007).
31. J. Demas, J. Manley, F. Tejera, H. Kim, F. M. Traub, B. Chen, A. Vaziri, High-speed, cortex-wide volumetric recording of neuroactivity at cellular resolution using light beads microscopy. *BioRxiv*, 02.21.432164 (2021).
32. D. A. Hartmann, A. A. Berthiaume, R. I. Grant, S. A. Harrill, T. Koski, T. Tieu, K. P. McDowell, A. V. Faino, A. L. Kelly, A. Y. Shih, Brain capillary pericytes exert a substantial but slow influence on blood flow. *Nat. Neurosci.* **24**, 633–645 (2021).
33. I. F. Smith, I. Parker, Imaging the quantal substructure of single IP_3R channel activity during Ca^{2+} puffs in intact mammalian cells. *Proc. Natl. Acad. Sci. U.S.A.* **106**, 6404–6409 (2009).
34. J. J. Iliff, M. Wang, Y. Liao, B. A. Plogg, W. Peng, G. A. Gundersen, H. Benveniste, G. E. Vates, R. Deane, S. A. Goldman, E. A. Nagelhus, M. Nedergaard, A paravascular pathway facilitates CSF flow through the brain parenchyma and the clearance of interstitial solutes, including amyloid. *Sci. Transl. Med.* **4**, 147ra111 (2012).
35. R. C. Brown, T. P. Davis, Calcium modulation of adherens and tight junction function: A potential mechanism for blood-brain barrier disruption after stroke. *Stroke* **33**, 1706–1711 (2002).
36. R. E. Dolmetsch, K. Xu, R. S. Lewis, Calcium oscillations increase the efficiency and specificity of gene expression. *Nature* **392**, 933–936 (1998).
37. H. Kosaka, Nitric oxide and hemoglobin interactions in the vasculature. *Biochim. Biophys. Acta* **1411**, 370–377 (1999).
38. J. Garthwaite, Concepts of neural nitric oxide–mediated transmission. *Eur. J. Neurosci.* **27**, 2783–2802 (2008).
39. B. Cauli, Cortical GABA interneurons in neurovascular coupling: Relays for subcortical vasoactive pathways. *J. Neurosci.* **24**, 8940–8949 (2004).

40. T. A. Longden, F. Dabertrand, D. C. Hill-Eubanks, S. E. Hammack, M. T. Nelson, Stress-induced glucocorticoid signaling remodels neurovascular coupling through impairment of cerebrovascular inwardly rectifying K^+ channel function. *Proc. Natl. Acad. Sci. U.S.A.* **111**, 7462–7467 (2014).
41. B. T. Drumm, G. W. Hennig, M. J. Battersby, E. K. Cunningham, T. S. Sung, S. M. Ward, K. M. Sanders, S. A. Baker, Clustering of Ca^{2+} transients in interstitial cells of Cajal defines slow wave duration. *J. Gen. Physiol.* **149**, 703–725 (2017).
42. D. J. Heredia, C.-Y. Feng, G. W. Hennig, R. B. Renden, T. W. Gould, Activity-induced Ca^{2+} signaling in perisynaptic Schwann cells of the early postnatal mouse is mediated by P2Y1 receptors and regulates muscle fatigue. *eLife* **7**, 909 (2018).

Acknowledgments: We acknowledge M. Ross and G. Kopec-Belliveau for excellent technical assistance. **Funding:** This study was supported by American Heart Association postdoctoral fellowships (14POST20480144 to T.A.L., 17POST33650030 to O.F.H., and 20POST35210155 to A.M.), an American Heart Association Scientist Development Grant (17SDG33670237 to T.A.L.), an American Heart Association Career Development Award (20CDA35310097 to O.F.H.), an American Heart Association Innovative Project Award (19IPLOI34660108 to T.A.L.), the Totman Medical Research Trust (to M.T.N.), the Fondation Leducq Transatlantic Network of Excellence on the Pathogenesis of Small Vessel Disease of the Brain (to M.T.N.), European Union's Horizon 2020 Research and Innovation Programme (grant agreement no. 666881, SVDs@target, to M.T.N.), the Henry M. Jackson Foundation for the Advancement of Military Medicine (HU0001-18-2-0016 to M.T.N.), and the NIH (P01-HL-095488, R01-HL-121706, R37-DK-053832, 7UM-HL-1207704, and R01-HL-131181 to M.T.N.). The NIH also provided support to T.A.L. (4P20 GM103644/4-5) via the Vermont Center on Behavior and Health (principal investigator: S. T. Higgins) and M.I.K. (R24HL120847 and R01HL120323). Support was also provided by the National Institute of Neurological Disorders and Stroke (NINDS) and National Institute on Aging (NIA) (R01NS110656 to M.T.N., R01AG066645 to T.A.L., and DP2OD02944801 to T.A.L.); the National Heart, Lung, and Blood Institute of the NIH (R35HL140027 to M.T.N.); the Vermont Center for Cardiovascular and Brain Health (P20-GM-135007 to M.T.N. and O.F.H.), and the University of California Irvine TMF Center (NCI-P30-CA062203). E.K. and G.M.K. received supported from the German Research Foundation (DFG)–funded Research Unit FOR2372 (KO 1582/10-1 and KO 1582/10-2 to E.K. and KO 902/17-1 and KO 902/17-2 to G.M.K.). The mouse strain *Cdh5*^{BAC}-GCaMP8 was created through the Cornell Heart Lung Blood Resource of Optogenetic Mouse Signaling (CHROMus; https://chromus.vet.cornell.edu). **Author contributions:** T.A.L. designed experiments, acquired and analyzed data, wrote the initial draft, and edited all subsequent drafts of the manuscript. G.W.H. developed analysis tools, analyzed imaging data, and edited the manuscript. A.M. acquired and analyzed data and edited the manuscript. O.F.H. acquired and analyzed data and edited the manuscript. E.K. and G.M.K. provided experimental reagents. M.I.K., B.S., F.K.L., J.C.L., and S.R. generated, phenotyped, and validated *Cdh5*^{BAC}-GCaMP8 mice. D.H.-E. edited the manuscript. M.T.N. directed the study and edited the manuscript. All authors reviewed the manuscript and approved its submission. **Competing interests:** The authors declare that they have no competing interests. **Data and materials availability:** All data needed to evaluate the conclusions in the paper are present in the paper and/or the Supplementary Materials. Additional data related to this paper may be requested from the authors.

Submitted 10 February 2021
Accepted 4 June 2021
Published 21 July 2021
10.1126/sciadv.abh0101

Citation: T. A. Longden, A. Mughal, G. W. Hennig, O. F. Harraz, B. Shui, F. K. Lee, J. C. Lee, S. Reining, M. I. Kotlikoff, G. M. König, E. Kostenis, D. Hill-Eubanks, M. T. Nelson, Local IP_3 receptor–mediated Ca^{2+} signals compound to direct blood flow in brain capillaries. *Sci. Adv.* **7**, eabh0101 (2021).

Science Advances

Local IP_3 receptor–mediated Ca^{2+} signals compound to direct blood flow in brain capillaries

Thomas A. Longden, Amreen Mughal, Grant W. Hennig, Osama F. Harraz, Bo Shui, Frank K. Lee, Jane C. Lee, Shaun Reining, Michael I. Kotlikoff, Gabriele M. König, Evi Kostenis, David Hill-Eubanks and Mark T. Nelson

Sci Adv **7** (30), eabh0101.
DOI: 10.1126/sciadv.abh0101